

## Pore-space alteration induced by brine acidification in subsurface geologic formations

Saeed Ovaysi<sup>1</sup> and Mohammad Piri<sup>1</sup>

Received 18 June 2013; revised 6 December 2013; accepted 20 December 2013; published 17 January 2014.

[1] A new Lagrangian particle-based method is presented to simulate reactive transport in natural porous media. This technique is based on Modified Moving Particle Semi-implicit (MMPS) and takes as input high-resolution voxel images of natural porous media. The flow field in the medium is computed by solving the incompressible Navier-Stokes equations. Moreover, a multicomponent ion transport model is coupled with a homogeneous and heterogeneous reactions module to handle pore-space alteration (i.e., pore-wall dissolution). The model is first successfully validated against the experimental data available in the literature. Subsequently, X-ray microtomographic images of two naturally occurring porous media are used to investigate the impact of reaction kinetics and pore-space topology on pore-space alteration induced by brine acidification in subsurface conditions. We observed that at the normal rates of reactions no significant change in porosity and permeability takes place in the short term. Whereas, higher reaction rates caused major changes in the macroscopic properties (e.g., porosity and permeability) of the rocks. We also show that these changes are strongly affected by the rocks' pore-scale topologies.

**Citation:** Ovaysi, S., and M. Piri (2014), Pore-space alteration induced by brine acidification in subsurface geologic formations, *Water Resour. Res.*, 50, 440–452, doi:10.1002/2013WR014289.

### 1. Introduction

[2] Subsequent to CO<sub>2</sub> injection into underground geological formations, a series of heterogeneous rock/fluid chemical reactions take place. These reactions, which also account for the permanent mineral trapping of carbon, gradually alter the pore-space topology of the rock formation. The resulting pore-space topology alterations translate into changes in the properties of the medium such as porosity and permeability. These changes affect fluids flow in the system and may have implications for the process. Clearly, it is highly desirable to avoid conditions whereby the rock structure undergoes changes favoring CO<sub>2</sub> leakage to the surface. Wellbore stimulation via acid injection in hydrocarbon reservoirs is another example where rock/fluid interactions play a critical role. In this case, unlike carbon sequestration, the objective is to enhance the permeability of the medium in order to improve production.

[3] These processes, despite their opposite objectives, are closely related as similar pore-scale physics dictate the outcomes. Therefore, a fundamental examination of the relevant phenomena at the pore scale can shed light on how to successfully implement the above-mentioned processes. Experimental investigation of pore-space dissolution due to

acid injection into carbonate rocks [Hoefner and Fogler, 1988; Fredd and Fogler, 1998; Golfier *et al.*, 2002; Luquot and Gouze, 2009] have provided valuable insights on the optimum conditions under which permeability enhancement is best achieved. In particular, Fredd and Miller [2000] present a classification of dissolution patterns based on injection flow rate. This subject is later expanded by Golfier *et al.* [2002], where a dissolution pattern diagram is presented to predict a priori the formation of wormholes using Peclet ( $Pe$ ) and Damkohler ( $Da$ ) dimensionless numbers. Similar classification of both dissolution and precipitation patterns is also reported by Daccord *et al.* [1993]. Furthermore, several experimental studies have focused on calcite precipitation in glass micromodels [Algive *et al.*, 2007; Yoon *et al.*, 2012] and flow cells [Katz *et al.*, 2011] to evaluate the impact of calcite deposition pattern on the porosity and permeability of the medium.

[4] Application of the above-mentioned findings in field-scale models requires an additional step to develop constitutive relations for Darcy-scale parameters that convey the correct physics. This may be achieved by further understanding the phenomena responsible for rock/fluid interactions at the pore scale. For example, Gouze and Luquot [2011] and Luquot and Gouze [2009] used X-ray microtomography to characterize changes in reactive surface area, porosity, and permeability at the pore scale induced by CO<sub>2</sub> injection into pure calcite rock samples. Pore-scale modeling of reactive transport is an alternative way to obtain relevant information to upscale [Kechagia *et al.*, 2002; Battiatto and Tartakovsky, 2011] these processes. Various numerical methods such as lattice Boltzmann [Sullivan *et al.*, 2005; Kang *et al.*, 2010; Chen *et al.*, 2013], pore-network modeling [Varloteaux *et al.*, 2013],

<sup>1</sup>Department of Chemical and Petroleum Engineering, University of Wyoming, Laramie, Wyoming, USA.

Corresponding author: S. Ovaysi, Institute for Computational Engineering and Sciences, University of Texas at Austin, 1 University Station C0200, ACES, Austin, TX 78712-0027, USA. (s.ovaysi@gmail.com)

and level set [Li *et al.*, 2008a] have been used to study mineral dissolution and precipitation in two-dimensional and three-dimensional porous media. Numerical schemes based on random walks and finite difference formulations have also been employed to study dissolution [Bekri *et al.*, 1995] and precipitation [Salles *et al.*, 1993] in artificially generated two-dimensional and three-dimensional porous media as well as fractures [Dijk and Berkowitz, 1998]. Conventional mesh-based methods [Yang *et al.*, 2013] such as finite volume have been applied to study pore-scale reactive transport with varied degrees of success [Molins *et al.*, 2012; Steefel and Maher, 2009].

[5] Despite these efforts, numerical simulation of reactive transport at the pore scale requires more research in two main areas: (a) inclusion of electrochemical migration in the transport equation and (b) development of robust algorithms to account for changes in pore-space topology induced by rock/fluid chemical reactions. As evidenced by Ovaysi and Piri [2013], electrochemical transport of ionic species is a critically important mechanism that cannot be ignored in a pore-scale model of reactive transport. Similar observations were made by Molins *et al.* [2012], where deviation of the results from experimental data at low pH was attributed to ignoring electrochemical migration in their model. Reliable simulation of flow and transport in systems with evolving solid boundaries is another area where more research is required. In this work, we focus on both of these areas.

[6] To this end, one can use mesh-based numerical techniques [Berger *et al.*, 2003; LeVeque and Li, 1994; Pember *et al.*, 1995; Miller and Trebotich, 2012]. These methods, however, require relatively significant improvements to handle changing boundary conditions expected at the pore scale in reactive systems. On the other hand, particle-based methods are potentially, due to their fully Lagrangian nature, capable of handling evolving rock/fluid boundaries more reliably. Among these techniques, Modified Moving Particle Semi-implicit (MMPS) [Ovaysi and Piri, 2010; Ovaysi, 2010; Ovaysi and Piri, 2011, 2012] and Smoothed Particle Hydrodynamics (SPH) [Monaghan, 2005; Tartakovsky *et al.*, 2008] have been applied to reactive transport problems. However, there are major differences between MMPS and SPH. First, the particle-based summations in SPH impose several assumptions on the quality of the kernel as well as the existence of a full support for the fluid particles. These restrictions significantly limit the ability of SPH to reliably deal with open flow boundaries. As a consequence, only periodic boundary conditions have been handled by SPH. The particle-based summations in MMPS, on the other hand, are less restrictive insofar as various boundary conditions on the open flow boundaries can be easily implemented [Ovaysi and Piri, 2010]. Another major difference is in the solution strategy: SPH solves the time-dependent governing equations in a fully explicit manner and relies on an artificial equation of state to simulate a quasi incompressible fluid; MMPS solves the governing equations semiimplicitly. Here, pressure is computed through the solution of an elliptic equation which is derived from the continuity equation for incompressible fluids. The above factors have enabled MMPS to be validated successfully against various experimental data [Ovaysi and Piri, 2010, 2011, 2013], whereas no such quantitative validations is available in the literature for SPH.

[7] In this paper, we present an extension of MMPS model to simulate pore-level reactive transport of fluids through naturally occurring porous media in order to enable the study of both of the above-mentioned areas. We first discuss the porous mediums studied in this work and the numerical discretization that would best suit MMPS. We then elaborate on the extended MMPS. This is followed by model validation against experimental results available in the literature. Finally, we present and analyze the simulation results followed by concluding remarks.

## 2. Pore-Space Representation

[8] In accordance with the objectives of this study, we selected two samples taken from rocks with different pore-space topologies, i.e., Gambier limestone (sample A) and Berea sandstone (sample B). Experimental measurements revealed 7800 mD and 980 mD permeabilities for the Gambier limestone and Berea sandstone, respectively. The measured porosities of these rocks are 49% and 22.7%, respectively. Since carbonates are more susceptible to rock/fluid reactions under subsurface conditions, we assumed that both of these rocks are completely composed of calcium carbonate. This assumption is not consistent with the mineralogy of Berea sandstone; nonetheless, a visual inspection of the X-ray microtomography images of these rocks, i.e., Figures 1 and 2, reveals vastly different pore-space topologies, see Blumenfeld *et al.* [2013] and Øren and Bakke [2003] for pore-size distributions. It is the impact of these different pore-space topologies on dissolution/precipitation patterns that we investigate in this work. Therefore, the original mineralogy of these rocks were not the main focus of the study. Furthermore, since the changes in porosity and permeability appear after long periods of time, we selected smaller samples to significantly reduce the time span of the simulations. We cut  $0.42 \text{ mm} \times 0.42 \text{ mm} \times 1.06 \text{ mm}$  samples from the original images. We then

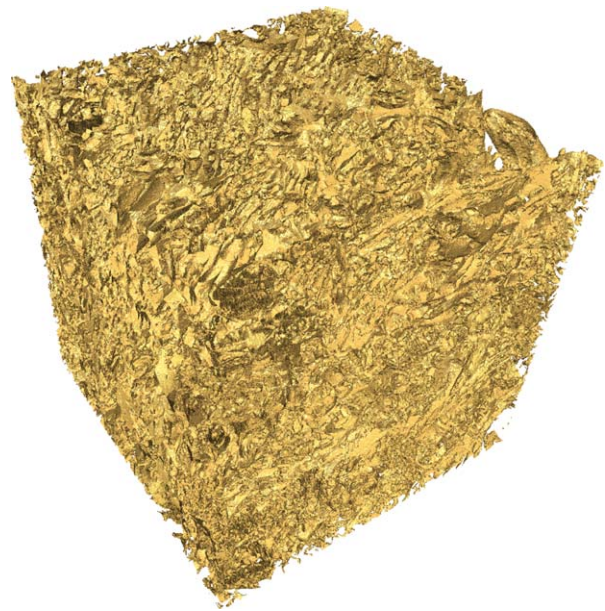


**Figure 1.** A  $(3.6 \text{ mm})^3$  isosurface of Gambier limestone at  $5.406 \text{ }\mu\text{m}$  resolution.



**Figure 2.** A  $(2.138 \text{ mm})^3$  isosurface of Berea sandstone at  $5.345 \text{ }\mu\text{m}$  resolution.

placed one particle in the center of each voxel of the discretized image, which provided a map to mark the solid/fluid particles. Figures 3 and 4 illustrate the void space occupied by fluid particles in the Gambier and Berea samples, respectively.

### 3. Particle-Based Summations

[9] To resolve the governing equations of flow and transport in a system represented by a set of  $i=1, \dots, N_p$  particles identified by their distance vector  $\mathbf{r}_i$ , one needs to define fairly accurate approximations of the differential operators used in those equations. The particle-based approximations presented in this section are those given in the original work by *Koshizuka et al.* [1995].

[10] Consider a continuous function  $A(\mathbf{r})$ . A particle-based approximation of this function can be written as

$$A_i = A(\mathbf{r}_i) = \frac{\sum_j^{N_i} A_j W(|\mathbf{r}_i - \mathbf{r}_j|)}{\sum_j^{N_i} W(|\mathbf{r}_i - \mathbf{r}_j|)} \quad (1)$$

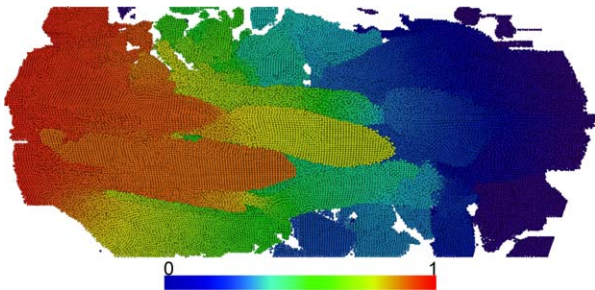


**Figure 3.** Distribution of static pressure (in Pa) in a  $0.42 \text{ mm} \times 0.42 \text{ mm} \times 1.06 \text{ mm}$  sample of Gambier limestone (sample A). Only the fluid particles are visualized.

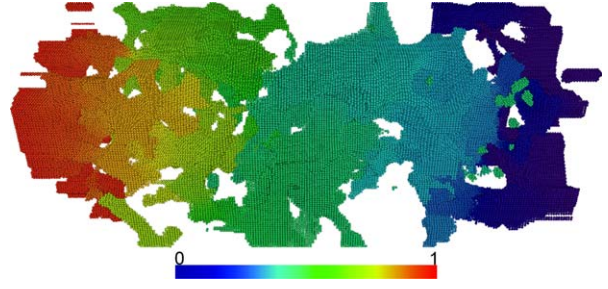


**Figure 4.** Distribution of static pressure (in Pa) in a  $0.42 \text{ mm} \times 0.42 \text{ mm} \times 1.06 \text{ mm}$  sample of Berea sandstone (sample B). Only the fluid particles are visualized.

where  $N_i$  is the total number of particles in the neighborhood of  $i$  and  $W$ , kernel, simply gives a higher weight to the particles close to  $i$  than those in distance. To reduce computational time and limit the number of neighboring particles, the kernel is usually chosen so that it adopts zero beyond a certain boundary. This boundary is called kernel size and denoted by  $h$ . One example of such a kernel that is used in the present work reads

$$W_{ij} = \begin{cases} -\left(\frac{2r}{h}\right)^2 + 2 & 0 \leq r < \frac{h}{2} \\ \left(\frac{2r}{h} - 2\right)^2 & \frac{h}{2} \leq r < h \\ 0 & r \geq h \end{cases} \quad (2)$$

where  $W_{ij} = W(r_{ij})$  and  $r = r_{ij} = |\mathbf{r}_i - \mathbf{r}_j|$ .

[11] Furthermore, in equations (3)–(5), we present the particle-based approximations of the gradient, divergence, and Laplacian operators, respectively, acting on particle  $i$ .

$$\nabla_i A = \frac{d}{N_i} \sum_j^{N_i} \frac{A_j - A_i}{r_{ij}^2} (\mathbf{r}_j - \mathbf{r}_i) W_{ij} \quad (3)$$

$$\nabla_i \cdot \mathbf{v} = \frac{d}{N_i} \sum_j^{N_i} \frac{(\mathbf{v}_j - \mathbf{v}_i) \cdot (\mathbf{r}_j - \mathbf{r}_i)}{r_{ij}^2} W_{ij} \quad (4)$$

$$\nabla_i^2 A = \frac{2d}{\lambda N_i} \sum_j^{N_i} (A_j - A_i) W_{ij} \quad (5)$$

where  $d$  is the number of spatial dimensions and the parameter  $\lambda$  is

$$\lambda = \frac{\int_V W(r) r^2 dv}{\int_V W(r) dv} \quad (6)$$

[12] Also,  $\mathcal{N}_i$ , particle number density, is defined as

$$\mathcal{N}_i = \sum_j^{N_i} W_{ij} \quad (7)$$

### 4. Model Description

[13] The transport of a reactive fluid through a porous medium is a complex process encompassing several

physicochemical processes. As such, a realistic pore-level reactive transport model must be able to address fluid flow, transport of charged and neutral species, and homogeneous and heterogeneous chemical reactions that result in pore-space alteration. In the previous studies, we have discussed the first three aspects of the model which we briefly explain here. We then complete the model description by discussing the heterogeneous fluid/rock reactions that lead to the alteration of the pore space.

#### 4.1. Fluid Flow

[14] The incompressible Navier-Stokes equations govern the pore-level laminar flow of a Newtonian incompressible fluid in porous media. Given the Lagrangian nature of MMPS, here we introduce the Lagrangian version of these equations. We begin by presenting the equation of motion, i.e.,

$$\frac{D\mathbf{v}}{Dt} = -\frac{1}{\rho}\nabla P_d - \frac{1}{\rho}\nabla P_s + \frac{\mu}{\rho}\nabla^2\mathbf{v} + \mathbf{g} \quad (8)$$

where  $\mathbf{v}$  is the velocity vector,  $\rho$  is density,  $\mu$  is viscosity,  $\mathbf{g}$  is the gravity vector,  $P_s$  is static pressure, and  $P_d$  is dynamic pressure. We consider the total pressure to be the summation of static and dynamic pressures, i.e.,  $P = P_s + P_d$ .

[15] MMPS follows a semiimplicit approach known as pressure projection method where the total velocity is represented by

$$\mathbf{v} = \mathbf{v}_E + \mathbf{v}_I \quad (9)$$

where subscripts  $E$  and  $I$  denote explicit and implicit, respectively.

[16]  $\mathbf{v}_E$  is computed using

$$\mathbf{v}_E = \mathbf{v}^n + \left( -\frac{1}{\rho}\nabla P_s + \frac{\mu}{\rho}\nabla^2\mathbf{v} + \mathbf{g} \right)^n \Delta t \quad (10)$$

where superscript  $n$  and  $\Delta t$  denote the previous time step and the size of time step, respectively.

[17] Static pressure in equation (10) is directly calculated using the external pressure gradient applied on the medium while taking into account its pore-space topology as implied by

$$\nabla^2 P_s = 0 \quad (11)$$

[18] The remainder of equation (8) is solved implicitly to compute  $\mathbf{v}_I$

$$\mathbf{v}_I = -\frac{\Delta t}{\rho}\nabla P_d \quad (12)$$

[19] To do that, the unknown field of  $P_d$  must be calculated using the continuity equation. However, to compensate for the errors resulting from the numerical operations, we present a modified continuity equation that takes into account minor deviations occurred in previous time steps, i.e.,

$$\frac{1}{\Delta t} \sum_{k=1}^n \nabla \cdot \mathbf{v}^k \Delta t^k + \nabla \cdot \mathbf{v} = 0 \quad (13)$$

[20] Combining equations (13), (9), and (12),  $P_d$  is obtained from

$$\nabla^2 P_d = \frac{\rho}{\Delta t} \left( \nabla \cdot \mathbf{v}_E + \frac{1}{\Delta t} \sum_{k=1}^n \nabla \cdot \mathbf{v}^k \Delta t^k \right) \quad (14)$$

[21] Further details regarding the above-mentioned equations are discussed elsewhere [Ovaysi and Piri, 2010]. The solution to these equations will resolve the pore-level flow of a single-component nonreactive fluid in porous media.

#### 4.2. Multicomponent Reactive Transport

[22] In addition to the equations described in section 4.1, transport of a multicomponent reactive fluid is also governed by

$$\frac{DC_i}{Dt} = \left( \frac{DC_i}{Dt} \right)_{\text{diffusion}} + \left( \frac{DC_i}{Dt} \right)_{\text{electrical coupling}} + \left( \frac{DC_i}{Dt} \right)_{\text{chemical reactions}} \quad (15)$$

where  $C_i$  is the molarity of species  $i$ .

[23] Equation (15) is solved explicitly at each time step for all species present in the system. Below, we discuss the three terms on the right-hand side of this equation, namely diffusion, electrical coupling, and chemical reactions.

##### 4.2.1. Diffusion

[24] The first term on the right-hand side of this equation refers to the contribution of molecular diffusion to the total transport and is computed by

$$\left( \frac{DC_i}{Dt} \right)_{\text{diffusion}} = D_i (\nabla^2 C_i + \nabla \cdot (C_i \nabla \ln \gamma_i)) \quad (16)$$

where  $D_i$  is the molecular diffusion coefficient and  $\gamma_i$  is the activity coefficient of species  $i$ . In this work, the activity coefficients of the neutral species are assumed to be unity whereas for the ions we use the Davies activity model [Samson *et al.*, 1999], i.e.,

$$\ln \gamma_i = -\frac{Az_i^2 \sqrt{I}}{1 + B\sqrt{I}} + Cz_i^2 I \quad (17)$$

where  $A$ ,  $B$ , and  $C$  are constants.  $z_i$  is the valence of the species  $i$  and  $I$ , ionic strength, is defined by

$$I = \sum_i^N C_i z_i^2 \quad (18)$$

where  $N$  is the total number of species.

##### 4.2.2. Electrical Coupling

[25] The different ions present in the system diffuse at different rates which can lead to an artificial state where the solution is electrically charged. To prevent this, the electrical coupling term must ensure that the electroneutrality condition always prevails at every point in the system, i.e.,

$$\sum_i^N z_i C_i = 0 \quad (19)$$

[26] The standard approach [Marchand *et al.*, 2001] to assure the electroneutrality condition is to solve the Poisson-Nernst-Planck equations. However, that approach

**Table 1.** The Homogeneous Reactions Used in This Study<sup>a</sup>

Index	Reaction	log $K_{eq}$
1	$\text{H}_2\text{O} \rightleftharpoons \text{H}^+ + \text{OH}^-$	-13.49
2	$\text{CO}_2 + \text{H}_2\text{O} \rightleftharpoons \text{H}_2\text{CO}_3$	-2.77
3	$\text{H}_2\text{CO}_3 \rightleftharpoons \text{HCO}_3^- + \text{H}^+$	-6.27
4	$\text{HCO}_3^- \rightleftharpoons \text{CO}_3^{2-} + \text{H}^+$	-10.16

<sup>a</sup>Equilibrium constants are taken from *Ellis et al.* [2010].

is computationally expensive and requires restrictions on the size of the time step. In a previous study [*Ovaysi and Piri*, 2013], we presented a new approach that delivers the same results at a lower computational cost. We suggest computing the electrical coupling term using

$$\left(\frac{DC_i}{Dt}\right)_{\text{electrical coupling}} = -\lambda z_i C_i \sum_j z_j C_j \quad (20)$$

where  $\lambda$  is calculated using

$$\lambda = \frac{\sum_i z_i C_i + \Delta t \sum_i z_i \left(\frac{DC_i}{Dt}\right)_{\text{diffusion}}}{\Delta t \sum_i z_i C_i \sum_i z_i^2 C_i} \quad (21)$$

which is obtained by combining equations (19), (20), and first-order time integration of  $C_i$ .

#### 4.2.3. Chemical Reactions

[27] Depending on their rate, chemical reactions can be categorized as equilibrium controlled or kinetics controlled. In the present work, we study the interaction of brine and calcite. Therefore, in Tables 2 and 1, we list seven chemical reactions that are believed to take place [*Chou et al.*, 1989]. We assume the four homogeneous reactions that are listed in Table 1 take place instantaneously and hence their equilibrium must be enforced at every point inside the fluid phase. On the other hand, the remaining three reactions, listed in Table 2, are heterogeneous surface reactions that proceed slowly according to their respective rate equations. First, we need to account for the equilibrium and kinetic reactions separately. To do that we write

$$\left(\frac{DC_i}{Dt}\right)_{\text{chemical reactions}} = \left(\frac{DC_i}{Dt}\right)_k + \left(\frac{DC_i}{Dt}\right)_{eq} \quad (22)$$

##### 4.2.3.1. Kinetic Reactions

[28] The kinetic reactions listed in Table 2 occur at the surface of the calcite crystals. In the present work, we assume that the flow field does not entrain the partially dissolved solid particles. Since the studied flow rates are low

( $Re \ll 1$ ), we believe this assumption is plausible. Furthermore, we assume the pore walls are completely made of calcite. Therefore, the reactive surface can easily be calculated by first marking the solid particles that interface with the fluid phase. A subset of these surface particles, i.e.,  $\mathbb{S}$ , can then be identified at the neighborhood of any fluid particle through the summations discussed in section 3. Also, since each particle represents a cubic grid of size  $D_p$ , original particle spacing, the volume occupied by each particle is calculated by  $V = \alpha D_p^3$ , where  $\alpha \geq 0$  is a shrinkage factor describing the size of particle compared to its original size. Also, the reactive surface of particle  $i$ ,  $A_i$ , is calculated through the assumption that particles shrink/grow homogeneously, i.e.,

$$A_i = 6\alpha_i^{\frac{2}{3}} D_p^2 \frac{\sum_{j \in \mathbb{F}} W_{ij}}{N_i} \quad (23)$$

where  $\mathbb{F}$  is a subset of particles in the neighborhood of  $i$  that includes only fluid particles. The summations in this equation are introduced to account for only the exposed surface of the solid particles.

[29] Also, the contribution of kinetic reactions in equation (22) for fluid particle  $i$  can be calculated using

$$\left(\frac{DC_{i,j}}{Dt}\right)_k = \frac{10^{-3}}{V_i N_i} \sum_{k \in \mathbb{S}} \sum_l R_{kj,l} A_k W_{ik} \quad (24)$$

where  $R_{kj,l}$  is the production rate of species  $j$  through the kinetic reaction  $l$  listed in Table 2 and  $N_r$  is the total number of kinetic reactions. All the variables of this equation are in SI system of units.

[30] To account for shrinkage/growth of the surface solid particles, we first calculate the amount of mass gained/lost as a result of the kinetic reactions, i.e.,

$$M_i = M_i + \frac{A_i \Delta t}{N_i} \sum_{k \in \mathbb{S}} \sum_l R_{k\text{CaCO}_3,l} A_k W_{ik} \quad (25)$$

where  $M$  is in mol. Then  $\alpha$  which is a measure of the extent of shrinkage/growth can be calculated by

$$\alpha = \frac{M_i}{\rho_{\text{CaCO}_3} D_p^3} \quad (26)$$

where  $\rho_{\text{CaCO}_3} = 27110 \text{ mol m}^{-3}$ .

[31] The shrinkage/growth of the solid particles continuously alters the pore space. This phenomenon is accounted for by introducing a modified kernel used in the particle-based summations discussed in section 3. Using a similar

**Table 2.** The Kinetic Reactions Used in This Study<sup>a</sup>

Index	Reaction	$-\frac{d\text{CaCO}_3}{dt}$ (mol cm <sup>-2</sup> s <sup>-1</sup> )
1	$\text{CaCO}_3 + \text{H}^+ \Rightarrow \text{Ca}^{2+} + \text{HCO}_3^-$	$8.9 \times 10^{-5} a_{\text{H}^+}$
2	$\text{CaCO}_3 + \text{H}_2\text{CO}_3^* \Rightarrow \text{Ca}^{2+} + 2\text{HCO}_3^-$	$5 \times 10^{-8} a_{\text{H}_2\text{CO}_3^*}$
3	$\text{CaCO}_3 \rightleftharpoons \text{Ca}^{2+} + \text{CO}_3^{2-}$	$6.5 \times 10^{-11} a_{\text{H}_2\text{O}} - 1.9 \times 10^{-2} a_{\text{Ca}^{2+}} a_{\text{CO}_3^{2-}}$

<sup>a</sup>Reaction rates are taken from *Chou et al.* [1989].

**Table 3.** Canonical Form of the Equilibrium Reactions

Index	Reaction	$K'_{eq}$
1	$\text{H}_2\text{O}-\text{H}^+ \rightleftharpoons \text{OH}^-$	$K_{eq,1}$
2	$\text{H}_2\text{O}+\text{CO}_2 \rightleftharpoons \text{H}_2\text{CO}_3$	$K_{eq,1}K_{eq,2}$
3	$\text{H}_2\text{O}+\text{CO}_2-\text{H}^+ \rightleftharpoons \text{HCO}_3^-$	$K_{eq,1}K_{eq,2}K_{eq,3}$
4	$\text{H}_2\text{O}+\text{CO}_2-2\text{H}^+ \rightleftharpoons \text{CO}_3^{2-}$	$K_{eq,1}K_{eq,2}K_{eq,3}K_{eq,4}$

concept presented earlier [Ovaysi and Piri, 2010], the modified kernel reads

$$W_{ij,\text{modified}} = \alpha_i \alpha_j W_{ij} \quad (27)$$

#### 4.2.3.2. Equilibrium Reactions

[32] The equilibrium reactions are treated according to the method described by Lichtner *et al.* [1996]. As the first step, the equilibrium reactions must be written in their canonical forms shown in Table 3. This leaves the primary and secondary species as listed in Table 4. Consider  $R'_{ej}$  the progress of the canonical reaction  $j$ , then for every secondary species  $i$

$$\left(\frac{DC_i}{Dt}\right)_{eq} = R'_{ei}, i=1, 2, 3, 4 \quad (28)$$

[33] Performing mass balance for primary species on the reactions listed in Table 3 reveals

$$\begin{aligned} \left(\frac{DC_5}{Dt}\right)_{eq} &= -R'_{e1} - R'_{e2} - R'_{e3} - R'_{e4} \\ \left(\frac{DC_6}{Dt}\right)_{eq} &= R'_{e1} + R'_{e3} + 2R'_{e4} \\ \left(\frac{DC_7}{Dt}\right)_{eq} &= -R'_{e2} - R'_{e3} - R'_{e4} \end{aligned} \quad (29)$$

[34] Substituting equation (28) in equation (29), we derive

$$\begin{aligned} \left(\frac{DC_5}{Dt}\right)_{eq} + \left(\frac{DC_1}{Dt}\right)_{eq} + \left(\frac{DC_2}{Dt}\right)_{eq} + \left(\frac{DC_3}{Dt}\right)_{eq} + \left(\frac{DC_4}{Dt}\right)_{eq} &= 0 \\ \left(\frac{DC_6}{Dt}\right)_{eq} - \left(\frac{DC_1}{Dt}\right)_{eq} - \left(\frac{DC_3}{Dt}\right)_{eq} - 2\left(\frac{DC_4}{Dt}\right)_{eq} &= 0 \\ \left(\frac{DC_7}{Dt}\right)_{eq} + \left(\frac{DC_2}{Dt}\right)_{eq} + \left(\frac{DC_3}{Dt}\right)_{eq} + \left(\frac{DC_4}{Dt}\right)_{eq} &= 0 \end{aligned} \quad (30)$$

[35] Also, from equations (15) and (22), we know

**Table 4.** Primary and Secondary Species

Secondary Index	Species	Primary Index	Species
1	$\text{OH}^-$	5	$\text{H}_2\text{O}$
2	$\text{H}_2\text{CO}_3$	6	$\text{H}^+$
3	$\text{HCO}_3^-$	7	$\text{CO}_2$
4	$\text{CO}_3^{2-}$		

$$\left(\frac{DC_i}{Dt}\right)_{eq} = \left(\frac{DC_i}{Dt}\right) - F_i(\mathbf{C}) \quad (31)$$

where

$$F_i(\mathbf{C}) = \left(\frac{DC_i}{Dt}\right)_{\text{diffusion}} + \left(\frac{DC_i}{Dt}\right)_{\text{electrical coupling}} + \left(\frac{DC_i}{Dt}\right)_k \quad (32)$$

can be known explicitly using the concentration values in the previous time step.

[36] Combining equations (30) and (31) yields

$$\begin{aligned} \left(\frac{D(C_5+C_1+C_2+C_3+C_4)}{Dt}\right) &= F_5(\mathbf{C}) + F_1(\mathbf{C}) + F_2(\mathbf{C}) + F_3(\mathbf{C}) \\ &\quad + F_4(\mathbf{C}) \\ \left(\frac{D(C_6-C_1-C_3-2C_4)}{Dt}\right) &= F_6(\mathbf{C}) - F_1(\mathbf{C}) - F_3(\mathbf{C}) - 2F_4(\mathbf{C}) \\ \left(\frac{D(C_7+C_2+C_3+C_4)}{Dt}\right) &= F_7(\mathbf{C}) + F_2(\mathbf{C}) + F_3(\mathbf{C}) + F_4(\mathbf{C}) \end{aligned} \quad (33)$$

[37] Using mass action equations for the reactions in Table 3, we obtain

$$\begin{aligned} C_1 &= \frac{K'_{eq,1} C_5 \gamma_5 C_t}{C_6 \gamma_6 \gamma_1} \\ C_2 &= \frac{K'_{eq,2} C_5 \gamma_5 C_7 \gamma_7}{\gamma_2 C_t} \\ C_3 &= \frac{K'_{eq,3} C_5 \gamma_5 C_7 \gamma_7}{C_6 \gamma_6 \gamma_3} \\ C_4 &= \frac{K'_{eq,4} C_5 \gamma_5 C_7 \gamma_7 C_t}{C_6^2 \gamma_6^2 \gamma_4} \end{aligned} \quad (34)$$

where  $C_t$  is the total molar concentration.

[38] Using equation (34) in equation (33), we reach at a set of three nonlinear equations. In the present work, we use Newton-Raphson method to solve for concentration of the primary species. Following that, concentration of the secondary species can also be known using equation (34).

[39] All the results presented in the following sections are generated using our parallel code on a hybrid multi-GPU platform with 54 GPUs.

## 5. Validation

[40] We validate the above model against a microfluidic reactive flow experiment performed by Li *et al.* [2008b]. For this purpose, we first generate a 4200  $\mu\text{m}$ -long medium of a cylindrical tube with 500  $\mu\text{m}$  diameter and 20  $\mu\text{m}$  resolution (see Figure 5). To replicate the experimental conditions, we assume the bordering solid particles to the tube in the middle 4000  $\mu\text{m}$  are completely made of calcite. The remaining length of the tube in the inlet and outlet is assumed to be nonreactive in compliance with the experimental setup that indicates ceramics. Next, water with 10 mM ionic strength (NaCl) and pH = 4 and 5 is injected to the tube at two different flow rates, i.e., 4.72 and

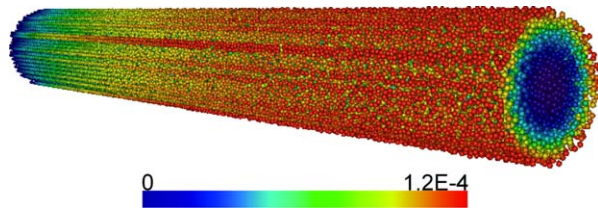


**Figure 5.** Visualization of  $\text{Ca}^{2+}$  molar concentration in the 4000  $\mu\text{m}$ -long reactive portion of a microtube at  $t = 15$  min. The image is obtained from our simulation results in this study when injecting a  $\text{pH} = 4$  solution at  $9.39 \mu\text{L}/\text{min}$  flow rate. Only the fluid particles are visualized.

$9.39 \mu\text{L}/\text{min}$ . To achieve these flow rates, we apply 0.19 and 0.38 Pa pressure difference across the length of the tube, respectively. Concentration of  $\text{Ca}^{2+}$  in the outlet stream is then recorded in each case after 15 min and plotted in Figure 6. As shown in this figure, our simulations produced comparable results with the experimental data and within the same range of accuracy of the modeling results presented in the same work, i.e., *Li et al.* [2008b]. It should be stressed that, in simulating the above experiment, only the reactions listed in Tables 1 and 2 were considered.

## 6. Results and Discussion

[41] The samples presented in section 2 are first saturated with water at a 1.2 M ionic strength ( $\text{NaCl}$  and  $\text{CaCl}_2$ ) and  $\text{pH} = 7$ . Then, at  $t = 0$  a highly acidic brine with  $\text{pH} = 1$  is continuously injected to the inlet of the samples. Brine concentrations are given in Table 5. Since the samples are entirely made of calcium carbonate, the heterogeneous reactions listed in Table 2 are expected to take place at the rock/fluid interfaces. We assume the process takes place under subsurface conditions of  $40^\circ\text{C}$  and 12.7 MPa [*Ellis et al.*, 2010], where  $\text{CO}_2$  exists as a super-critical phase. Molecular diffusion coefficients of the ions involved are given in Table 6.

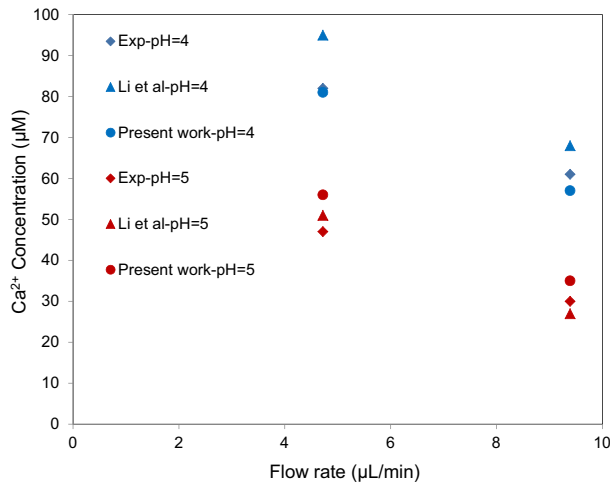


**Figure 6.** Comparison of  $\text{Ca}^{2+}$  concentration in the outlet after 15 min as measured in the experiments, modeling results from *Li et al.* [2008b], and our simulation results in the present work.

**Table 5.** Brine Compositions in mol/L

Component	Initial Brine	Acidic Brine
$\text{H}_2\text{O}$	55.56	55.56
$\text{H}^+$	$1\text{e}-7$	0.1
$\text{Na}^+$	0.9	0.9
$\text{Ca}^{2+}$	0.1	0.1
$\text{Cl}^-$	1.1	1.2

### 6.1. Kinetics

[42] To study the impact of kinetics on pore-space alteration, the acidic brine is injected to sample A under two different conditions. In case I, the kinetic reactions take place under the normal rates reported in Table 2. Whereas, the kinetic reaction rates for case II were  $100\times$  faster than the normal rates. Other variables such as the equilibrium constants and hydrodynamic conditions were identical in both cases. The applied pressure difference across the length of the sample is 1 Pa. Under these conditions, we calculate  $Pe = \frac{ul}{D_{\text{H}^+}} = 3.4$  and  $Re = \frac{\rho ul}{\mu} = 0.03$ , where  $u$  is the mean interstitial velocity and  $l$  is the specific length calculated using the following analysis [*Ovaysi and Piri*, 2011]. Knowing both the permeability and grain size of Berea sandstone [*Øren and Bakke*, 2003], a virtual grain size of 800  $\mu\text{m}$  is estimated for Gambier limestone through  $K \propto a^{1.4}$ , where  $K$  and  $a$  denote permeability and grain size, respectively [*Shepherd*, 1989]. Although grain size is of no physical meaning in a limestone, we use this number as a measure for specific length to determine the hydrodynamics and dispersion regimes under which the simulations are performed. Also, to have a rough estimate of dissolution pattern inside the sample, we define

$$Da = \frac{\text{rate of dissolution}}{\text{rate of convection}} = \frac{\psi_{\text{CaCO}_3}}{\rho_M Q} \quad (35)$$

where  $\psi_{\text{CaCO}_3} = \frac{dM}{dt}$  is the rate of rock dissolution and  $M$  is the molar mass of the dry sample.  $\rho_M$  and  $Q$  denote molar density and volume flow rate of the injected acidic brine, respectively. Although, due to variation of permeability and reactive surface area,  $Da$  changes continuously over time, we obtain an average  $Da = 2.47$  and 9.24 for cases I and II, respectively. Note the above  $Pe$  indicates a transitional dispersion zone where molecular diffusion coefficient plays a significant role. This is evidenced by a uniform distribution and hence the absence of concentration gradient of  $\text{H}^+$  ions across the width of the pores in Figure 7. Furthermore, a  $Da = 2.47$  implies that even under the normal reaction rates, transport of acid to the rock

**Table 6.** Molecular Diffusion Coefficients of Different Ions in Water at  $40^\circ\text{C}$  Taken From *Ellis et al.* [2010] and *Newman and Thomas-Alyea* [2004]

Species	$D_m (\text{m}^2/\text{s}) \times 10^9$	Species	$D_m (\text{m}^2/\text{s}) \times 10^9$
$\text{H}^+$	9.312	$\text{CO}_2$	1.94
$\text{OH}^-$	5.26	$\text{H}_2\text{CO}_3$	1.5
$\text{Na}^+$	1.334	$\text{HCO}_3^-$	1.24
$\text{Ca}^{2+}$	0.792	$\text{CO}_3^{2-}$	0.968
$\text{Cl}^-$	2.032		

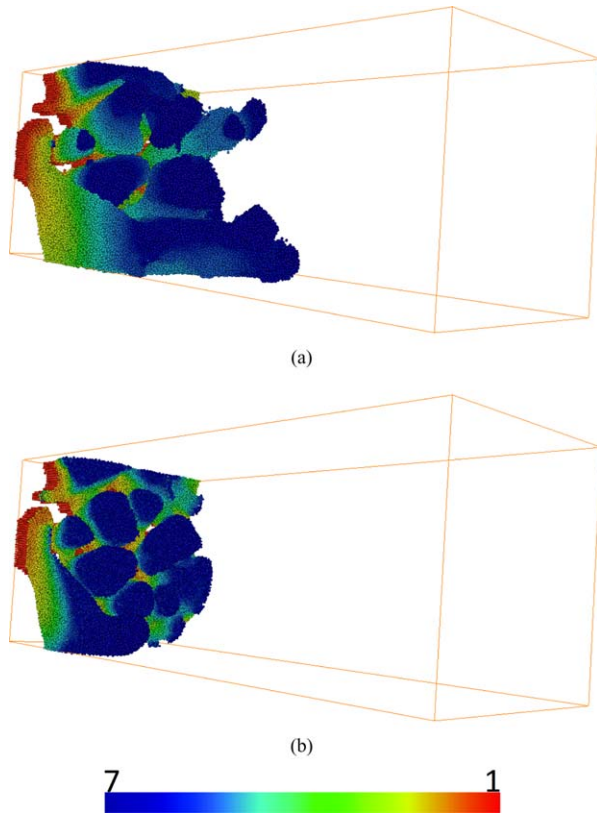


**Figure 7.** pH distribution at  $t = 20$  s in sample A with (a) normal kinetics and (b)  $100\times$  heightened kinetics. Only the fluid particles with  $\text{pH} < 2$  are shown.

surface is inferior to the rate by which the acid is consumed on the rock surface. In other words, the actual rate of kinetic reactions is controlled by the transport of reactants and reaction products to and from the rock-fluid surface. Therefore, a  $100\times$  increase in the rate of kinetic reactions will not be proportionally translated into higher dissolution of the rock matrix. Instead, only a  $3.7\times$  increase in the rate of dissolution is observed. Also, notable in this figure is the slower progress of the  $\text{H}^+$  plume in case II. This is due to the higher rate of  $\text{H}^+$  consumption in the  $100\times$  heightened kinetic reactions which leaves less  $\text{H}^+$  to be transported downstream. Therefore, the acidic front dissolves more and travels less into the sample. In Figure 8, we illustrate how this phenomenon affects the dissolution pattern. As clearly seen, higher reaction rates have led to more dissolution of the inlet pore walls in Figure 8. However, this fast rate of dissolution has consumed most of the  $\text{H}^+$  ions and, consequently, the pore walls in the downstream are less affected when compared to Figure 8 where the kinetic reactions are slower. Comparing the variation of rock surface areas for the above cases in Figure 15, it becomes clear that the dissolution pattern in case II is localized at the inlet of the sample. In case I, on the other hand, the dissolution process takes place more uniformly throughout the medium. Therefore, the rate of rock dissolution in case I does not increase sharply as in case II. Given that rock dissolution in both cases is transport limited, this can be directly attributed to the continuous supply of  $\text{H}^+$  ions throughout the sample in

case I where rock dissolution takes place in regions far away from the inlet, see Figure 15. This localized dissolution pattern is in agreement with previous studies where a similar behavior was observed both at the core scale [Golfier *et al.*, 2002; Gouze and Luquot, 2011] and field scale [Kalia and Balakotaiah, 2007; Cohen *et al.*, 2008]. Although normal reaction rates yield a uniform dissolution pattern, the magnitude of this dissolution during the time span of our simulations is small and its impact on porosity and permeability of the sample is insignificant. The faster kinetics, on the other hand, cause significant change in both porosity and permeability as shown in Figure 9. In this figure, we plot the normalized porosities and permeabilities of sample A versus time. The normalized porosities and permeabilities are obtained based on their respective values computed in the absence of chemical reactions. It is shown that gradual dissolution of the pore walls leads to an imbalance between the inlet and outlet flow rates where the inlet flow rate has to be greater in order to fill the newly created pore space. To highlight this, in Figure 9 we have plotted both the inlet and outlet permeabilities. Note that calcium carbonate can both precipitate and dissolve. However, the highly acidic environment inside the medium forces dissolution to be dominant, i.e., we did not observe  $\alpha > 1$ . This leads to a net  $\text{CO}_2$  production in the medium. However, the  $\text{CO}_2$  content of the brine remains below its solubility limit reported by Ellis *et al.* [2010].

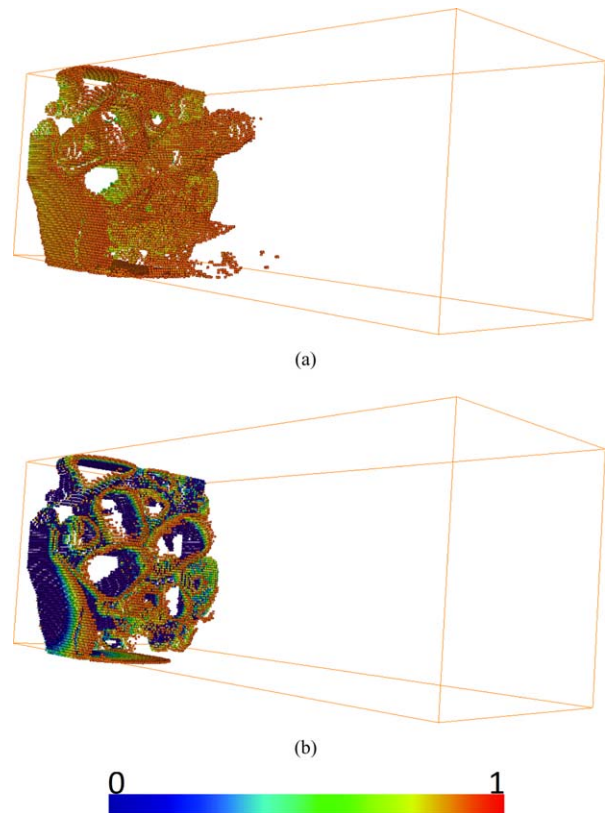


**Figure 8.** Shrinkage/growth factor  $\alpha$  for the solid particles in sample A at  $t = 20$  s under (a) normal kinetics and (b)  $100\times$  heightened kinetics. Only the solid particles with  $\alpha < 0.95$  are shown.

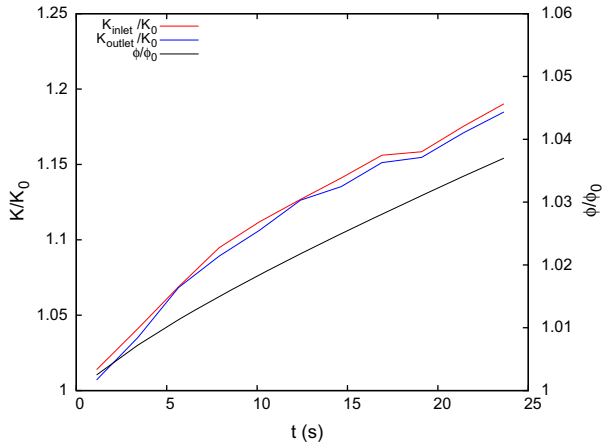


**Figure 9.** Variation of porosity and permeability in sample A during the injection of a highly acidic brine with  $100\times$  faster kinetics.

## 6.2. Pore-Space Topology

[43] Sample B presents a medium with drastically different pore-scale features than that of sample A and hence a suitable candidate to investigate the impact of these features on pore-space alteration. Identical to section 6.1, we inject a highly acidic brine into sample B that is initially saturated with a neutral brine by applying a 1 Pa pressure difference across the length of the sample. Furthermore, to observe a noticeable alteration of the pore space, the kinetic reactions were sped up  $100\times$ . This compares to case II in the previous section. As expected, the low permeability of sample B hinders progress of the acidic brine through the sample, see Figure 10. Using a  $200\ \mu\text{m}$  grain size for Berea sandstone [Øren and Bakke, 2003], we calculated a  $Re = 0.009$  and  $Pe = 0.1$  which places the dispersion regime well within the region dominated by molecular diffusion. Under this regime, the acidic brine diffuses through the fluid channels it comes in contact with regardless of their conductivity. This implies that the less conductive (passive) flow channels have an equal chance of coming in contact with the acidic brine as the more conductive (active) channels. The acidic brine can then dissolve the

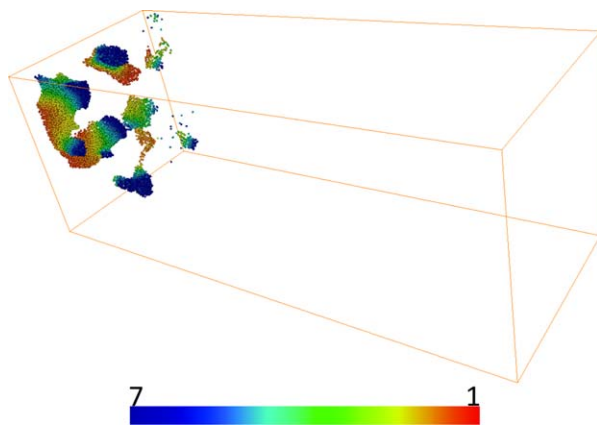


**Figure 10.** pH distribution at  $t = 18\ \text{s}$  in sample B with  $100\times$  heightened kinetics. Only the fluid particles with  $\text{pH} < 2$  are shown.

walls of the exposed narrow channels creating new active conduits and hence improving the permeability of the medium. The above phenomenon is demonstrated in Figure 11 where we illustrate the active flow channels in sample B at different times during the simulation. Note that dissolution of the solid walls in the marked area gives birth to a new active flow conduit which connects to the main flow channel in the medium. Once the acidic brine diffuses through the sample and reaches the narrow conduit that connects the large pore on top to the main flow channel, it gradually widens the conduit. After some time, this widened conduit acts as a reliable connection between the large pore on top and the main flow channel. In Figure 11, a similar phenomenon has created another active flow channel just below the marked area. The collective impact of these new active flow channels translates to a significant improvement in permeability of sample B as shown in Figure 12. Noteworthy, creation of new active flow channels in sample B has led to a situation where a minor change in porosity yields a significant change in permeability. This is also evidenced by the relatively insignificant amount of pore-wall dissolution seen in Figure 13 when compared with that in sample A, cf. Figure 8, which is also demonstrated in Figures 14 and 15. Also noteworthy in Figure 12, the inlet permeability grows much more quickly than the outlet permeability. This is to pull more fluid particles into the medium to supplant the dissolved solid walls. However, since sample B has a much lower permeability than that of sample A, the gap between the inlet and outlet permeabilities are wider in Figure 12 when compared with Figure 9.

[44] Using equation (35) we calculate  $Da = 62.6$  which compared to case II in section 6.1 is a much larger number and implies a faster rate of rock matrix dissolution. This can be mainly attributed to susceptibility of the pore space in sample B to the creation of new flow channels and, hence, a greater exposure of the rock surface to the acidic brine which further speeds up the dissolution process. The existence of large well-connected pores in sample A makes the creation of new flow channels less likely. Instead, the main mechanism by which pore-wall dissolution contributes to porosity/permeability alteration is by widening of the already existing channels, see Figure 16. Note that this process creates a flow pattern where more fluid has to be injected into the medium. Mass conservation implies that more fluid has to pass faster through the same unaltered conduits downstream of the medium. It is this increase in velocity that translates to a more actively connected porous medium in Figure 16b. Furthermore, it is important to note that the dissolution process gradually smooths the pore walls, leading to a gradual decrease in the surface area available for further dissolution. This in turn leads to a gradual decline in the rate of dissolution. Formation of new channels can enhance this process by introducing sharp decreases in the rock surface area. As shown in Figure 15, the surface area available to the kinetic reactions in sample B decreases rapidly after 5 s into the simulation which is caused by the formation of new channels. This process brings some of the inactive pores in contact with a supply of acidic brine. Therefore, as evidenced in the above figure, rate of dissolution increases rather sharply after 5 s. This process continues until  $t = 10\ \text{s}$  when the newly created channels have been widened enough to be visible in

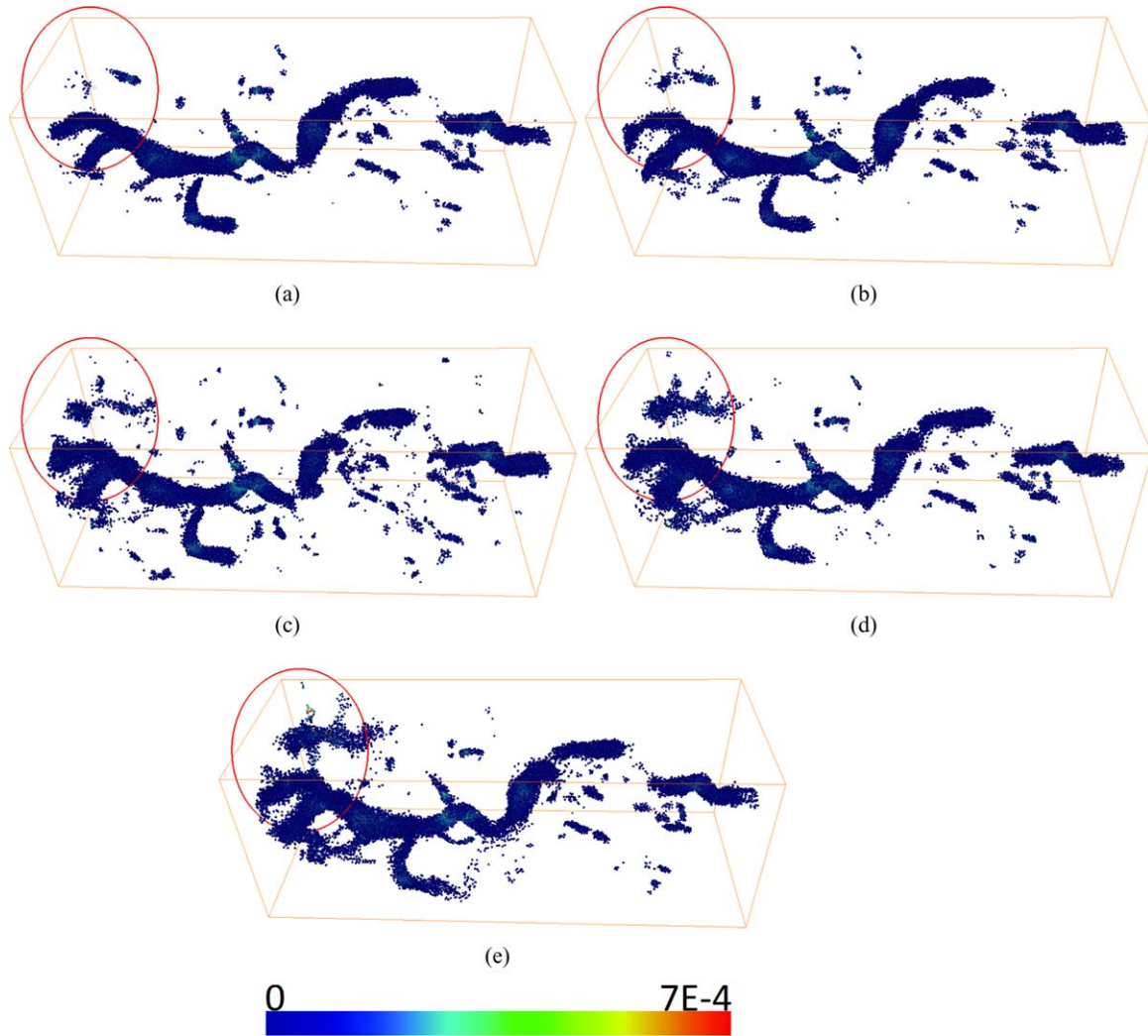


**Figure 11.** The active flow channels in sample B at (a) 2 s, (b) 6 s, (c) 10 s, (d) 14 s, and (e) 18 s. Only the particles faster than  $7 \times 10^{-5}$  m/s are shown. The color bar indicates velocity in m/s.

Figure 11. These channels are then connected to the main flow channel. Upon establishing the connections, permeability of the medium increases sharply, see Figure 12.

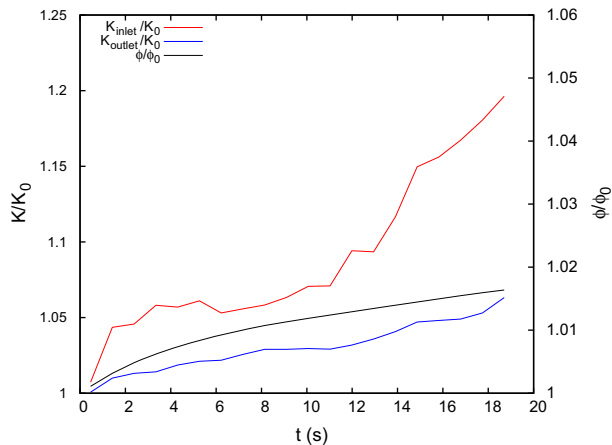


**Figure 12.** Variation of porosity and permeability in sample B during the injection of a highly acidic brine at  $100\times$  faster kinetics.

After this point, the dissolution process slows down due to the decreased surface area available for reactions. Note that permeability enhancement in sample B after  $t = 10$  s is mainly due to widening of the pore channels which is the sole mechanism responsible for permeability enhancement in sample A.

### 6.3. Constitutive Relations for Permeability and Surface Area

[45] The quantities computed in our pore-scale simulations can be used to propose constitutive relations describing the evolution of permeability and rock surface area as a function of variation in porosity in the samples studied.

*Luquot and Gouze* [2009] propose  $\frac{\sigma}{\sigma_0} = \left(\frac{\phi}{\phi_0}\right)^a$  to account for the variation of specific surface area  $\sigma = \frac{A}{(1-\phi)V}$  versus porosity. In this equation,  $V$  is the bulk volume of the sample and subscript 0 denotes the initial conditions. Given that  $V$  is constant, to find the power law exponent  $a$ , in Figure 17 we fit our data to  $\frac{A}{A_0} = \frac{1-\phi}{1-\phi_0} \left(\frac{\phi}{\phi_0}\right)^a$  to get  $a = -7.05$ ,  $-3.48$ , and  $-2.77$  for case I sample A, case II sample A, and case II sample B, respectively. Clearly, reaction surface

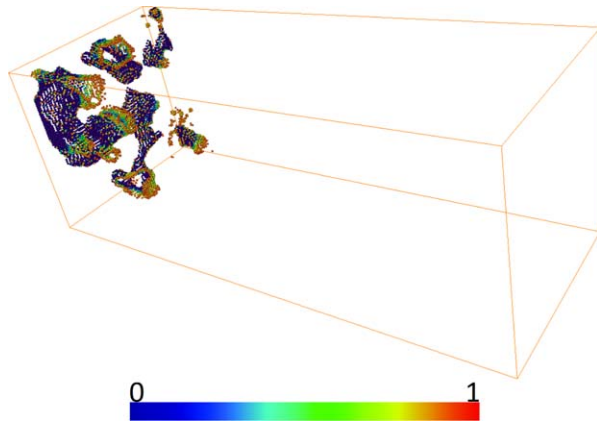


**Figure 13.** Shrinkage/growth factor  $\alpha$  for the solid particles in sample B at  $t = 18$  s under  $100\times$  heightened kinetics. Only the solid particles with  $\alpha < 0.95$  are shown.

area in sample A is more sensitive to changes in porosity for case I. However, this sensitivity is not proportionally translated to permeability enhancement as noted earlier. On the contrary, in sample B where reduction in surface area versus porosity is much milder, we observe the highest enhancement in permeability, cf. Figure 18. Furthermore, since permeability enhancement in this sample is nonlinear, we found that the power law exponent in  $K \propto \phi^b$  [Carman, 1937] is a function of porosity variation. Given our earlier discussion regarding the birth of new flow channels in sample B after 10 s into the simulation, we calculated  $b = 1.13$  for  $t < 10$  s and  $b = 14.1$  for  $t > 10$  s which is consistent with previous studies on this subject [Noiriel et al., 2004]. Permeability variation in case II sample A, on the other hand, is more uniform and we obtained  $b = 5.76$  for the entire time span of the simulation. One should note that applicability of these relations to larger samples of these rock types is a subject for further investigation.

## 7. Conclusions

[46] In this study, we presented a technique to model pore-space alteration caused by rock/fluid chemical interactions. The new model is built on the MMPS platform which is a Lagrangian, direct pore-scale modeling technique. Two rock samples, namely Berea sandstone and Gambier limestone, possessing vastly different pore-scale topologies, were imaged using X-ray microtomography. Furthermore, since carbonates are more reactive in acidic environments, it was assumed that both of these rocks are made of calcium carbonate only. We then injected a highly acidic brine into these samples and using normal reaction rates, we did not observe any noticeable alteration of the pore space in 20 s (real time). Since the main objective of this study was to present a Lagrangian pore-scale modeling technique that is capable of handling changing rock-fluid boundaries that occur during acid injection into carbonate rocks, we artificially created circumstances where rock-fluid boundaries did change; namely, the kinetic rock/fluid reactions were sped up  $100\times$ . This enabled us to reach our goal of investigating the impact of chemical pore-space alterations on the rocks macroscopic properties in a practical amount of time.

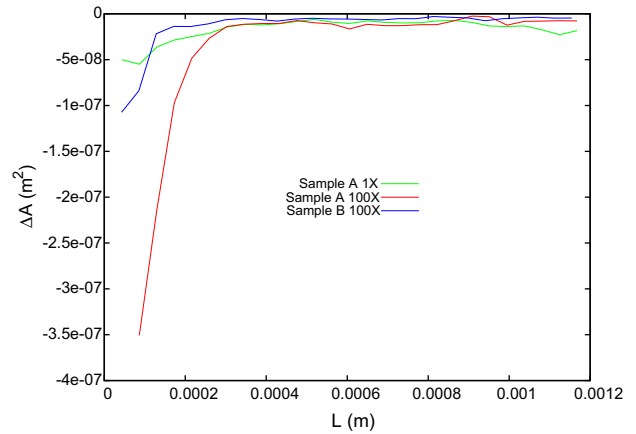


**Figure 14.** Variation of rock surface area along the length of samples A (cases I and II) and B (case II) at  $t = 18$  s. The acidic brine is injected at  $L = 0$ .

The results revealed that pore-scale features play a significant role on the type of pore-space alterations that are induced by rock/fluid chemical reactions. Those in turn determine the changes in macroscopic properties such as porosity and permeability. We observed that the dissolution caused by the exposure of pore walls to acidic brine leads to the widening of the exposed pores. In the medium where the most conductive flow channels are connected to the rest of the system through narrow pores, pore wall dissolution can significantly enhance permeability. This significant enhancement in permeability, however, is not necessarily accompanied by a significant increase in porosity. On the other hand, if the porous medium is well-connected through a network of conductive flow channels, widening of the already conductive pores is the main mechanism by which permeability is enhanced. This implies that a considerable change in porosity has to occur before we note a major improvement in permeability.

[47] The simulations carried out in this study covered a dispersion regime where molecular diffusion is dominant.

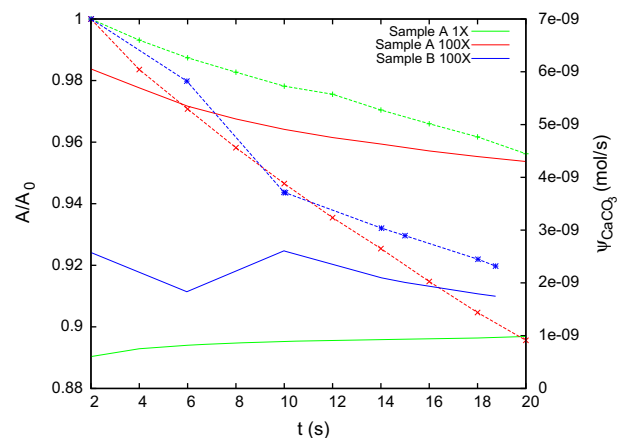


**Figure 15.** Evolution of rock surface area (dashed lines with symbols) and dissolution rate (solid lines) over time in samples A (cases I and II) and B (case II). The initial reaction surface areas in samples A and B are  $1.28 \times 10^{-5} \text{ m}^2$  and  $7.18 \times 10^{-6} \text{ m}^2$ , respectively.

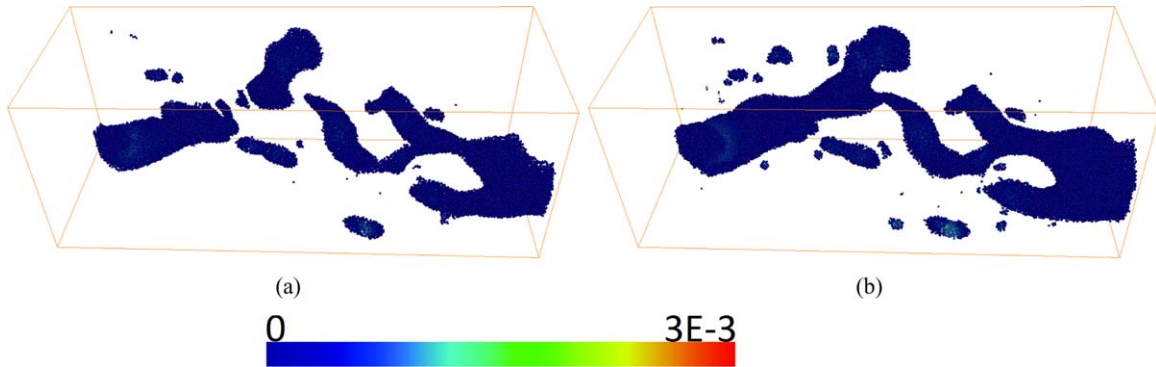


**Figure 16.** The active flow channels in sample A at (a) 2 s and (b) 20 s. Only the particles faster than  $3 \times 10^{-4}$  m/s are shown. The color bar indicates velocity in m/s.

This means that all the pore-scale channels that lie on an equal distance in the pore space from the injection site are equally exposed to the acidic brine. At high Peclet numbers, however, the injected acidic brine prefers the more conductive channels and hence the chances for pore-wall dissolution in those channels increase. At the same time, the less conductive channels are rarely exposed to the acidic brine. This can significantly modify the dissolution pattern in porous media at high Peclet numbers. A future work should shed light on this aspect of pore space alteration at high Peclet numbers.

[48] We also presented constitutive relations describing the variations in permeability and reaction surface area with changes in porosity for the samples studied here. However, we note that one would need to investigate their applicability for larger samples. Even though, this question has been partly answered for single component transport in small pore-scale samples, see *Ovaysi and Piri* [2011], the subject still requires more investigation due to complex processes involved in reactive transport.

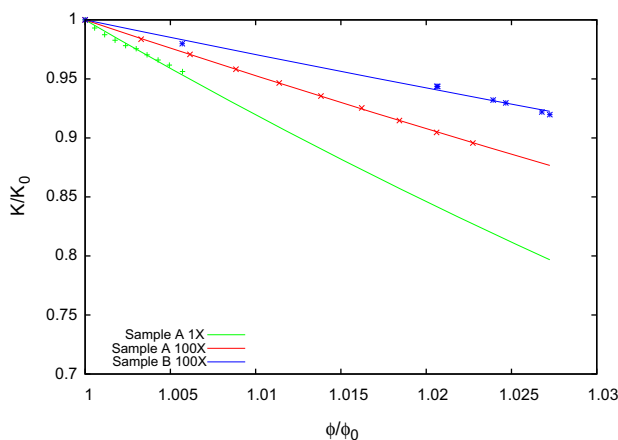


**Figure 17.** Variation of reaction surface area versus porosity in samples A (cases I and II) and B (case II). Dots represent the simulation results whereas the lines are obtained by fitting those results to  $\frac{A}{A_0} = \frac{1-\phi}{1-\phi_0} \left(\frac{\phi}{\phi_0}\right)^a$ . Exponent  $a$  is  $-7.05$  (sample A case I),  $-3.48$  (sample A case II), and  $-2.77$  (sample B case II).

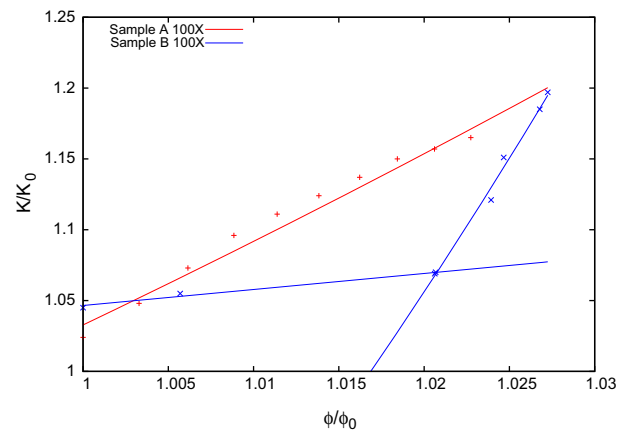


**Figure 18.** Variation of the rate of rock dissolution over time in sample A and B (both case II). Dots represent the simulation results whereas the line is obtained by fitting those results to  $K = c + \left(\frac{\phi}{\phi_0}\right)^b$ . For sample A, we obtain  $(c, b) = (0.033, 5.76)$  whereas for sample B we calculate  $(c, b) = (0.047, 1.13)$  at  $t < 10$  s and  $(c, b) = (-0.27, 14.1)$  at  $t > 10$  s.

[49] **Acknowledgments.** We gratefully acknowledge financial support of Encana and the School of Energy Resources and the Enhanced Oil Recovery Institute at the University of Wyoming.

## References

- Algive, L., S. Bekri, M. Robin, and O. Vizika (2007), Reactive transport: Experiments and modeling, paper presented at the International Symposium Society of Core Analysts, Institut Français du Pétrole, Calgary, Canada.
- Battiato, I., and D. M. Tartakovsky (2011), Applicability regimes for macroscopic models of reactive transport in porous media, *J. Contam. Hydrol.*, 120–121, 18–26.
- Bekri, S., J. F. Thovert, and P. M. Adler (1995), Dissolution of porous media, *Chem. Eng. Sci.*, 50(17), 2765–2791.
- Berger, M. J., C. Helzel, and R. J. Leveque (2003), h-box methods for the approximation of hyperbolic conservation laws on irregular grids, *SIAM J. Numer. Anal.*, 41(3), 893–918.
- Blumenfeld, R., M. Blunt, B. Bijeljic, E. Boek, O. Gharbi, P. Mostaghimi, and A. Raeni (2013), Imperial College consortium on pore-scale modeling, Yearly Progress Report, 3 Jan. Imperial College, London, U. K.
- Carman, P. (1937), Fluid flow through granular beds, *Trans. Inst. Chem. Eng.*, 15, 150–166.
- Chen, L., Q. Kang, B. A. Robinson, Y. L. He, and W. Q. Tao (2013), Pore-scale modeling of multiphase reactive transport with phase transitions

- and dissolution-precipitation processes in closed systems, *Phys. Rev. E*, *87*, 043306.
- Chou, L., R. M. Garrels, and R. Wollast (1989), Comparative study of the kinetics and mechanisms of dissolution of carbonate minerals, *Chem. Geol.*, *78*, 269–282.
- Cohen, C. E., D. Ding, M. Quintard, and B. Bazin (2008), From pore scale to wellbore scale: Impact of geometry on wormhole growth in carbonate acidization, *Chem. Eng. Sci.*, *63*, 3088–3099.
- Daccord, G., O. Lietard, and R. Lenormand (1993), Chemical dissolution of a porous medium by a reactive fluid—II. Convection vs reaction, behavior diagram, *Chem. Eng. Sci.*, *48*(1), 179–186.
- Dijk, P., and B. Berkowitz (1998), Precipitation and dissolution of reactive solutes in fractures, *Water Resour. Res.*, *34*(3), 457–470.
- Dullien, F. A. L. (1992), *Porous Media: Fluid Transport and Pore Structure*, Academic, San Diego, Calif.
- Ellis, B. R., L. E. Crandell, and C. A. Peters (2010), Limitations for brine acidification due to SO<sub>2</sub> co-injection in geologic carbon sequestration, *Int. J. Greenhouse Gas Control*, *4*, 575–582.
- Freddi, C. N., and H. S. Fogler (1998), Influence of transport and reaction on wormhole formation in porous media, *AIChE J.*, *44*(9), 1933–1949.
- Freddi, C. N., and M. J. Miller (2000), Validation of carbonate matrix stimulation models, paper presented at the SPE International Symposium on Formation Damage Control, Soc. of Pet. Eng., Lafayette, La.
- Golfier, F., C. Zarcone, B. Bazin R. Lenormand, D. Lasseux, and M. Quintard (2002), On the ability of a Darcy-scale model to capture wormhole formation during the dissolution of a porous medium, *J. Fluid Mech.*, *457*, 213–254.
- Gouze, P., and L. Luquot (2011), X-ray microtomography characterization of porosity, permeability and reactive surface changes during dissolution, *J. Contam. Hydrol.*, *120–121*, 45–55.
- Hoefner, M. L., and H. S. Fogler (1988), Pore evolution and channel formation during flow and reaction in porous media, *AIChE J.*, *34*(1), 45–54.
- Kalia, N., and V. Balakotaiah (2007), Modeling and analysis of wormhole formation in reactive dissolution of carbonate rocks, *Chem. Eng. Sci.*, *62*, 919–928.
- Kang, Q., P. C. Lichtner, and D. R. Janecky (2010), Lattice Boltzmann method for reacting flows in porous media, *Adv. Appl. Math. Mech.*, *2*(5), 545–563.
- Katz, G. E., B. Berkowitz, A. Guadagnini, and M. W. Saaltink (2011), Experimental and modeling investigation of multicomponent reactive transport in porous media, *J. Contam. Hydrol.*, *120–121*, 27–44.
- Kechagia, P. E., I. N. Tsimpanogiannis, Y. C. Yortsos, and P. Lichtner (2002), On the upscaling of reaction-transport processes in porous media with fast or finite kinetics, *Chem. Eng. Sci.*, *57*, 2565–2577.
- Koshizuka, S., H. Tamako, and Y. Oka (1995), A particle method for incompressible viscous flow with fluid fragmentation, *Comput. Fluid Dyn. J.*, *4*(1), 29–46.
- LeVeque, R. J., and Z. L. Li (1994), The immersed interface method for elliptic equations with discontinuous coefficients and singular sources, *SIAM J. Numer. Anal.*, *31*(4), 1019–1044.
- Li, X., H. Huang, and P. Meakin (2008a), Level-set simulation of coupled advection-diffusion and pore structure evolution due to mineral precipitation in porous media, *Water Resour. Res.*, *44*, W12407, doi:10.1029/2007WR006742.
- Li, L., C. I. Steefel, and L. Yang (2008b), Scale dependence of mineral dissolution rates within single pores and fractures, *Geochim. Cosmochim. Acta*, *72*, 360–377.
- Lichtner, P. C., C. I. Steefel, and E. H. Oelkers (1996), *Reactive Transport in Porous Media*, Mineral. Soc. of Am., Chantilly VA, USA.
- Luquot, L., and P. Gouze (2009), Experimental determination of porosity and permeability changes induced by injection of CO<sub>2</sub> into carbonate rocks, *Chem. Geol.*, *265*, 148–159.
- Marchand, J., E. Samson, and J. J. Beaudoin (2001), Modeling ion transport mechanisms in unsaturated porous media, National Research Council Canada, Report No. NRCC-44698, p. 1–18.
- Miller, G. H., and D. Trebotich (2012), An embedded boundary method for the Navier-Stokes equations on a time-dependent domain, *Commun. Appl. Math. Comput. Sci.*, *7*(1), 1–31.
- Monaghan, J. J. (2005), Smoothed particle hydrodynamics, *Rep. Prog. Phys.*, *68*, 1703–1759.
- Molins, S., D. Trebotich, C. I. Steefel, and C. Shen (2012), An investigation of the effect of pore scale flow on average geochemical reaction rates using direct numerical simulation, *Water Resour. Res.*, *48*, W03527, doi:10.1029/2011WR011404.
- Newman, J., and K. E. Thomas-Alyea (2004), *Electrochemical Systems*, John Wiley, Hoboken, N. J.
- Øren, P.-E., and S. Bakke (2003), Reconstruction on Berea sandstone and pore-scale modeling of wettability effects, *J. Pet. Sci. Eng.*, *39*, 177–199.
- Noiriel, C., P. Gouze, and D. Bernard (2004), Investigation of porosity and permeability effects from microstructure changes during limestone dissolution, *Geophys. Res. Lett.*, *31*, L24603, doi:10.1029/2004GL021572.
- Ovaysi, S., and M. Piri (2010), Direct pore-level modeling of incompressible fluid flow in porous media, *J. Comput. Phys.*, *229*, 7456–7476.
- Ovaysi, S. (2010), Direct pore-level modeling of fluid flow in porous media, PhD dissertation, Dep. Chem. Pet. Eng., Univ. of Wyoming, Wyo.
- Ovaysi, S., and M. Piri (2011), Pore-scale modeling of dispersion in disordered porous media, *J. Contam. Hydrol.*, *124*, 68–81.
- Ovaysi, S., and M. Piri (2012), Multi-GPU acceleration of direct pore-scale modeling of fluid flow in natural porous media, *Comput. Phys. Commun.*, *183*, 1890–1898.
- Ovaysi, S., and M. Piri (2013), Pore-scale dissolution of CO<sub>2</sub>+SO<sub>2</sub> in deep saline aquifers, *Int. J. Greenhouse Gas Control*, *15*, 119–133.
- Pember, R. B., J. B. Bell, P. Colella, W. Y. Crutchfield, and M. L. Welcome (1995), An adaptive Cartesian grid method for unsteady compressible flow in irregular regions, *J. Comput. Phys.*, *120*(2), 278–304.
- Salles, J., J. F. Thovert, and P. M. Adler (1993), Deposition in porous media and clogging, *Chem. Eng. Sci.*, *48*(16), 2839–2858.
- Samson, E., G. Lemaire, J. Marchand, and J. J. Beaudoin (1999), Modeling chemical activity effects in strong ionic solutions, *Comput. Mater. Sci.*, *15*, 285–294.
- Shepherd, R. G. (1989), Correlations of permeability and grain size, *Ground Water*, *27*(5), 633–638.
- Steefel, C. I., and K. Maher (2009), Fluid-rock interaction: A reactive transport approach, *Rev. Mineral. Geochem.*, *70*, 485–532.
- Sullivan, S. P., F. M. Sani, M. L. Johns, and L. F. Gladden (2005), Simulation of packed bed reactors using lattice Boltzmann methods, *Chem. Eng. Sci.*, *60*(12), 3405–3418.
- Tartakovsky, A. M., G. Redden, P. C. Lichtner, T. D. Scheibe, and P. Meakin (2008), Mixing-induced precipitation: Experimental study and multiscale numerical analysis, *Water Resour. Res.*, *44*, W06S04, doi:10.1029/2006WR005725.
- Varloteaux, C., M. T. Vu, S. Bekri, and P. M. Adler (2013), Reactive transport in porous media: Pore-network model approach compared to pore-scale model, *Phys. Rev. E*, *87*, 023010.
- Yang, X. F., T. D. Scheibe, M. C. Richmond, W. A. Perkins, S. J. Vogt, S. L. Codd, J. D. Seymour, and M. I. McKinley (2013), Direct numerical simulation of pore-scale flow in a bead pack: Comparison with magnetic resonance imaging observations, *Adv. Water Resour.*, *54*, 228–241.
- Yoon, H., A. J. Valocchi, C. J. Werth, and T. Dewers (2012), Pore-scale simulation of mixing-induced calcium carbonate precipitation and dissolution in a microfluidic pore network, *Water Resour. Res.*, *48*, W02524, doi:10.1029/2011WR011192.